PHYSICAL REVIEW FLUIDS **3**, 034201 (2018)

Nanoparticle motion on the surface of drying droplets

Mingfei Zhao and Xin Yong[*]

Department of Mechanical Engineering, Binghamton University, State University of New York, Binghamton, New York 13902, USA

(Received 13 December 2017; published 28 March 2018)

Advances in solution-based printing and surface patterning techniques for additive manufacturing demand a clear understanding of particle dynamics in drying colloidal droplets and its relationship with deposit structure. Although the evaporation-driven deposition has been studied thoroughly for the particles dispersed in the bulk of the droplet, few investigations have focused on the particles strongly adsorbed to the droplet surface. We modeled the assembly and deposition of the surface-active particles in a drying sessile droplet with a pinned contact line by the multiphase lattice Boltzmann-Brownian dynamics method. The particle trajectory and its area density profile characterize the assembly dynamics and deposition pattern development during evaporation. While the bulk-dispersed particles continuously move to the contact line, forming the typical "coffee-ring" deposit, the interface-bound particles migrate first toward the apex and then to the contact line as the droplet dries out. To understand this unexpected behavior, we resolve the droplet velocity field both in the bulk and within the interfacial region. The simulation results agree well with the analytical solution for the Stokes flow inside an evaporating droplet. At different stages of evaporation, our study reveals that the competition between the tangential surface flow and the downward motion of the evaporating liquid-vapor interface governs the dynamics of the interface-bound particles. In particular, the interface displacement contributes to the particle motion toward the droplet apex in a short phase, while the outward advective flow prevails at the late stage of drying and carries the particles to the contact line. The final deposit of the surface-adsorbed particles exhibits a density enhancement at the center, in addition to a coffee ring. Despite its small influence on the final deposit in the present study, the distinct dynamics of surface-active particles due to the interfacial confinement could offer a new route to deposition control when combined with Marangoni effects.

DOI: 10.1103/PhysRevFluids.3.034201

I. INTRODUCTION

Evaporation-driven self-assembly and deposition of colloidal materials has been recognized as a promising way for preparing functional nanomaterials [1,2], patterning surfaces for biological and chemical sensors [3–6], and printing high-performance optical and electronic devices [7–10]. In these applications, the functionality and performance of nanomaterials, sensors, and devices are critically determined by the deposited colloidal structures. Deposition patterns [4,11–13] obtained upon the drying of a colloidal droplet are surprisingly plentiful, which are governed by the complex interplay of multiple factors, such as substrate wetting properties [4,14], temperature [15], solvent composition [16–18], and physicochemical properties of particles [19]. The "coffee ring" is perhaps the most famous example, which exhibits substantially higher particle density along the perimeter of the deposit [11]. This inhomogeneous pattern is often undesirable in many applications and thus prompts

---

[*] xyong@binghamton.edu

extensive research efforts on its formation mechanisms [11,15,19–22]. Advective hydrodynamics in the bulk of a sessile droplet developed during evaporation has been widely accepted as the main driver for the coffee ring [11,21,23], since colloidal particles are typically homogeneously dispersed inside the droplet. If dry particles can be directly delivered to and adsorbed irreversibly at the liquid-vapor interface (e.g., by electrospray technique [24]), the surface flow instead of the bulk flow will govern the dynamics of particles confined at the droplet surface and the deposition pattern may be altered. However, our understanding of the flow field is incomplete on the droplet surface. Its influence on particle dynamics and assembly at the free surface and the subsequent deposition structure remain largely unexplored. Direct experimental probe of the surface-adsorbed particle motion has been rarely reported [25], mainly due to the continuously moving and curved free surface of a drying droplet. Thus, the numerical modeling provides a promising way to reveal the interplay between the surface flow and the particle dynamics during droplet evaporation.

In this paper, we investigate the evaporation-induced particle self-assembly and deposition using numerical simulations, and reveal the relationship between the final deposition pattern and the initial particle distribution in the droplet. Of particular interest is how the surface flow of the drying droplet modulates the assembly and deposition of particles that are adsorbed only at the interface. We apply a two-way coupled lattice Boltzmann-Brownian dynamics (LB-BD) method to simulate three-dimensional (3D) colloidal sessile droplets under isothermal and quasisteady evaporation. The lattice Boltzmann method (LBM) has been developed as an efficient and promising tool to simulate multiphase flow problems [26–29]. However, modeling coexisting phases with density and viscosity contrasts (e.g., liquid-vapor systems) is still a challenging problem for the LBM [29–40] due to the density variations across the liquid-vapor interface, which severely compromise the numerical stability of the simulation. Nonetheless, the local density change could play an important role in the dynamics of the particles adsorbed at the interface. Thus, we exploit a hybrid LB-BD method to model 3D fluids with density contrast [36], taking advantage of the recently developed two-dimensional (2D) framework [41]. More importantly, we invent a scheme to control the contact line motion during evaporation, especially to achieve contact line pinning. The ability of modeling an evaporating droplet with a pinned contact line permits faithful reproduction of the coffee-ring effect in the simulation.

In the discussion below, we first detail the two-way coupled 3D multiphase LB-BD method with density contrast and the boundary conditions for evaporation and contact line pinning. Using this model, we examine the assembly and deposition of the interface-bound particles and compare the results against the ones for the particles in the bulk. We elucidate the complex dynamics of the surface-adsorbed particles by analyzing the evaporation-driven flow field. From these results, we reveal that the physical confinement of the evaporating liquid-vapor interface contributes significantly to the particle motion at the free surface, which leads to an enhancement in particle density at the center of droplet footprint.

II. NUMERICAL METHOD

A. 3D multiphase lattice Boltzmann model with density contrast

The hydrodynamics of a binary fluid laden with particles under isothermal conditions [36] is described by the continuity equation [Eq. (1)], the Navier-Stokes equation [Eq. (2)], and the Cahn-Hilliard equation [Eq. (3)]:

$$\frac{\partial \rho_0}{\partial t} + \rho \nabla \cdot \vec{u} = 0, \tag{1}$$

$$\frac{\partial (\rho \vec{u})}{\partial t} + \nabla \cdot (\rho \vec{u}\vec{u}) = -\nabla p + \nabla \{\eta [\nabla \vec{u} + (\nabla \vec{u})^T]\} - \phi \nabla \mu_\phi + \vec{F}, \tag{2}$$

$$\frac{\partial \phi}{\partial t} + \nabla \cdot (\phi \vec{u}) = \theta_{\mathrm{M}} \nabla^2 \mu_\phi. \tag{3}$$

Here ρ_0 is the average fluid density that determines the pressure field according to the ideal gas law as $p = \rho_0 c_\mathrm{s}^2$, where c_s is the speed of sound, ρ is the local density that varies between the liquid density ρ_l and the vapor density ρ_v, η is the dynamic viscosity, and $\vec{u}$ is the local fluid velocity. The local order parameter ϕ represents the fluid phases, namely, ρ is linearly dependent on ϕ as $\rho{=}\rho_\mathrm{l}(\phi + \phi^*)/2\phi^* - \rho_\mathrm{v}(\phi - \phi^*)/2\phi^*$, where $\phi^* = (\rho_\mathrm{l} - \rho_\mathrm{v})/2$ is the equilibrium order parameter. According to the relation, the local order parameters of values ϕ^* and $-\phi^*$, respectively, represent the liquid and vapor phase, while $\phi = 0$ indicates the interface position. $\vec{F}$ is the external body forcing term applied to the fluid due to the presence of particles. θ_M is the mobility of the order parameter field whose transport is governed by the chemical potential.

The chemical potential of the binary fluid with particles is defined as $\mu_\phi{=}A(4\phi^3 - 4\phi^{*2}\phi) - \kappa\nabla^2\phi + \partial\psi_\mathrm{p}/\partial\phi$, where the first and second terms represent the contributions of the bulk phases and the interface, respectively. The thickness of interface W and surface tension σ are described in terms of parameters A and κ as $W = \sqrt{2\kappa/A}/\phi^*$ and $\sigma = 4\sqrt{2\kappa A}\phi^{*3}/3$. ψ_p is the free energy density describing the particle-fluid interaction, given by $\psi_\mathrm{p}(\vec{r},t) = \sum_i V_0 \exp(-|\vec{r} - \vec{r}_i|/r_0)[\phi(\vec{r},t) - \phi_i]^2$ [41–43]. The summation represents the influence of all nearby particles on the fluid at the discrete lattice position $\vec{r}$. ϕ_i is the order parameter of the ith particle at the continuous off-lattice position $\vec{r}_i$, which defines its wetting behavior. V_0 dictates the interaction strength, and r_0 controls both the range and strength of the interaction.

The above governing equations are discretized by the LBM into two lattice Boltzmann equations (LBEs) [Eqs. (4) and (5)] [36,37]:

$$f_i(\vec{x} + \vec{e}_i\delta t, t + \delta t) = f_i(\vec{x},t) - \frac{1}{\tau_f}\left[f_i(\vec{x},t) - f_i^\mathrm{eq}(\vec{x},t)\right] + \left(1 - \frac{1}{2\tau_f}\right)\delta t\frac{(\vec{e}_i - \vec{u})}{c_\mathrm{s}^2}\left[\nabla\rho c_\mathrm{s}^2(\Gamma_i - \omega_i) - \phi\nabla\mu_\phi\Gamma_i + \vec{F}\Gamma_i\right], \tag{4}$$

$$g_i(\vec{x} + \vec{e}_i\delta t, t + \delta t) = g_i(\vec{x},t) - \frac{1}{\tau_g}\left[g_i(\vec{x},t) - g_i^\mathrm{eq}(\vec{x},t)\right]. \tag{5}$$

Here $\Gamma_i = \omega_i[1 + (\vec{e}_i \cdot \vec{u})/c_\mathrm{s}^2 + (\vec{e}_i \cdot \vec{u})^2/2c_\mathrm{s}^4 - |\vec{u}|^2/2c_\mathrm{s}^2]$ and $c_\mathrm{s} = 1/\sqrt{3}$ is the speed of sound in the LBM. τ_f and τ_g are the respective relaxation times for the two LBEs. $\vec{e}_i$ is the lattice velocity, which indicates the direction of the particle distribution functions f and g at a certain lattice node. For the D3Q19 velocity discretization, we have

$$\vec{e}_i = \begin{cases} (0,0,0) & i = 0 \\ (1,0,0),(-1,0,0),(0,1,0),(0,-1,0),(0,0,1),(0,0,-1) & i = 1\text{–}6 \\ (1,1,0),(-1,1,0),(1,-1,0),(-1,-1,0), & i = 7\text{–}10 \\ (1,0,1),(-1,0,1),(1,0,-1),(-1,0,-1), & i = 11\text{–}14 \\ (0,1,1),(0,-1,1),(0,1,-1),(0,-1,-1) & i = 15\text{–}18 \end{cases}.$$

The corresponding weighting factors ω_i are $\omega_0 = 1/3, \omega_{1\text{–}6} = 1/18, \omega_{7\text{–}18} = 1/36$. The average density is defined as $\rho_0 = \vec{u} \cdot \nabla\rho\delta t/2 + \sum_i f_i$, and the local order parameter is obtained as $\phi = \sum_i g_i$. The momentum with local density is calculated from $\rho\vec{u} = -\phi\nabla\mu_\phi\delta t/2 + \vec{F}\delta t/2 + \sum_i f_i\vec{e}_i$. The equilibrium distribution functions f^eq and g^eq are calculated from the macroscopic variables [36,44]: $f_i^\mathrm{eq} = \omega_i\rho_0 + \rho(\Gamma_i - \omega_i)$ and $g_i^\mathrm{eq} = \omega_i[B_i + \phi(3\vec{e}_i \cdot \vec{u})/c_\mathrm{s}^2]$, where $B_0 = [\phi - (1 - \omega_0)3\tilde{M}\mu_\phi/c_\mathrm{s}^2]/\omega_0$, $B_i|_{i\neq 0} = (3\tilde{M}\mu_\phi)/c_\mathrm{s}^2$, and the numerical mobility parameter is $\tilde{M}$. The relationship between the mobility θ_M and the numerical mobility parameter $\tilde{M}$ is given as $\tilde{M} = \theta_\mathrm{M}/[(\tau_g - 0.5)\delta t]$. The dynamic viscosity is related to the relaxation time as $\eta = c_\mathrm{s}^2\rho(\tau_f - 0.5)$. Importantly, the difference $-\nabla(p - \rho c_\mathrm{s}^2)$ is introduced to the LBE as the forcing term [36] in order to correctly recover the Navier-Stokes equation for multiphase flow with density contrast. Unless otherwise stated, the first- and second-order spatial derivatives of the macroscopic properties are calculated using the isotropic finite difference scheme [32].

B. Two-way particle-fluid coupling and particle dynamics

Accounting for the particle-fluid interaction, the fluid body force $\vec{F}$ consists of the viscous drag force $\vec{G}^{\mathrm{drag}}$ and the force $\vec{G}$ associated with the wettability of particles. $\vec{G}^{\mathrm{drag}}$ is obtained as $\vec{G}^{\mathrm{drag}} = -\sum_i \delta(\vec{r}-\vec{r}_i)\vec{F}^{\mathrm{drag},i}$, where $\delta(\vec{r})$ is the Dirac delta function and $\vec{F}^{\mathrm{drag},i} = -\zeta(\vec{r}_i)[\delta\vec{r}_i/\delta t - \vec{u}(\vec{r}_i,t)]$ is the drag force acting on the ith particle. $\zeta(\vec{r}_i) = 6\pi\eta(\vec{r}_i)R_{\mathrm{p}}$ is the Stokes's drag coefficient for a particle with radius R_{p}, and $\eta(\vec{r}_i) = c_s^2\rho(\vec{r}_i)(\tau_f - 0.5)$ is the local dynamic viscosity, which varies with the particle position across the liquid-vapor interface. $\vec{G}$ is calculated from $\vec{G} = \sum_i \vec{f}_i(\vec{r},t)$, where $\vec{f}_i(\vec{r},t) = 2V_0\phi\nabla\exp(-|\vec{r}-\vec{r}_i|/r_0)[\phi(\vec{r},t)-\phi_i]$.

Considering negligible inertia of small particles, their dynamics is described by the overdamped Langevin equation as follows [41,43]:

$$d\vec{r}_i = \vec{u}_i(\vec{r}_i,t)\,dt + \sqrt{D_{\mathrm{p}}(\vec{r}_i)}\,d\vec{W}(t) + \frac{dt}{\zeta(\vec{r}_i)}\big[\vec{F}_i^{\mathrm{f}}(t) + \vec{F}_i^{\mathrm{pp}}(t)\big]. \tag{6}$$

Particle positions are updated through Eq. (6) by using a second-order Runge-Kutta method [43]. $D_{\mathrm{p}}(\vec{r}_i) = (k_{\mathrm{B}}T)/[6\pi R_{\mathrm{p}}\eta(\vec{r}_i)]$ is the particle diffusion coefficient, and $\vec{W}(t)$ is a Gaussian random variable with variance $\langle|\vec{W}(t+dt)-\vec{W}(t)|^2\rangle = 6\,dt$, which satisfies the fluctuation-dissipation theorem. $\vec{F}_i^{\mathrm{f}}(t) = \int d\vec{r}\,\vec{f}_i(\vec{r},t)$ is the total force on the ith particle from the surrounding fluid. $\vec{F}_i^{\mathrm{pp}}$ is the particle-particle interaction force defined as

$$\vec{F}_i^{\mathrm{pp}}(t) = -\sum_{j=1,\,j\neq i}^{N} \partial\psi_{\mathrm{m}}(|\vec{r}_i-\vec{r}_j|)/\partial(|\vec{r}_i-\vec{r}_j|). \tag{7}$$

The summation runs over all the neighboring j particles. For the particles in the liquid phase, the repulsive Morse potential is used in this work to represent the excluded volume effect:

$$\psi_{\mathrm{m}}(r) = \varepsilon_{\mathrm{rep}}\{1-\exp\left[-\lambda(r-r_{\mathrm{e}})\right]\}^2 \text{ for } r < r_{\mathrm{e}}, \tag{8}$$

where $\varepsilon_{\mathrm{rep}}$ and λ determine the strength and range of repulsion, respectively. r_{e} is the specific distance where the force between particles is equal to zero. The attractive force among particles in the vapor phase is also described by Eq. (8) for $r > r_{\mathrm{e}}$ with a much smaller $\varepsilon_{\mathrm{att}}$. The attraction between particles and the wall is along the normal direction (the y direction) and expressed by $F_{i,y}^{w}(t) = \partial\psi_w(\Delta r_{i,y})/\partial(\Delta r_{i,y})$, where $\Delta r_{i,y}$ is the particle-wall distance. A similar Morse potential [45] $\psi_{\mathrm{w}}(r) = \varepsilon\{1-\exp[-\lambda(r-r_{\mathrm{a}})]\}^2$ for $r < r_{\mathrm{a}}$ is used for the wall attraction. Other details about the two-way coupling between fluid and particles and the particle dynamics were described in our previous work [41].

C. Evaporation, symmetric boundary conditions, and contact line pinning

We induce the evaporation of liquid masses under isothermal conditions with low evaporation rates by imposing a Dirichlet boundary condition on the order parameter $\phi|_{S_{\mathrm{H}}} = \phi_{\mathrm{H}}$, where S_{H} is an evaporation boundary enclosing the system and the order parameter at the boundary $\phi_{\mathrm{H}} < -\phi^*$ [41,46]. We assign the value $\phi_{\mathrm{H}} = -1.1\phi^*$ outside a hemispherical surface with a radius of 38 LB units enclosing a sessile droplet. The computational phase transition model for the LBM has been discussed in a number of papers [41,46–49]. The evaporation model in the work uses the phase field gradient to induce net evaporative flux, thereby driving droplet evaporation [41,46]. This approach simulates diffusion-dominated evaporation under isothermal and quasisteady assumptions, owing to the absence of energy equation [46,50]. We also note that the use of free-energy LBM is debatable when phase change occurring at the liquid-vapor interface [49]. However, previous simulations have shown that this method produces physical hydrodynamics and evaporation behavior consistent with experiments and theoretical models [41,46,50–52] in the limit of a high thermal conductivity of liquid and negligible thermal Marangoni effects. Despite these idealized conditions, the simulation

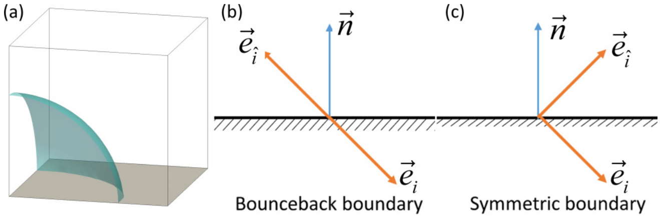

FIG. 1. (a) Representative simulation box with the symmetric boundary conditions applied to all four horizontal boundaries for simulating a quarter droplet. The schematic diagrams of the directional change of the particle distribution functions at the (b) bounce-back boundary and (c) symmetric boundary, where $\vec{e}_i$ represents the incoming direction and $\vec{e}_{\hat{i}}$ is the outgoing direction at the boundary. $\vec{n}$ is the boundary normal toward the fluid.

allows one to isolate a pure hydrodynamic driving forces on the particle assembly and deposition, which offers unique insight.

Moreover, it is well known that the thermal, surfactant, and solutal Marangoni effects [15,17,53,54] can produce complex flow structures in drying droplets and significantly influence the deposition pattern. A physical system is likely subject to one or more of these Marangoni effects. However, only the thermal Marangoni effect induced by the differential evaporation and substrate heat transfer is present in an ideal, single-component droplet [53,55]. Previous studies have shown that the thermal Marangoni flow for a water droplet evaporating at room temperature is negligible compared to the evaporation-driven bulk flow toward the contact line [15]. Thus, we try to model a simple system in this study by not considering various Marangoni effects.

With the aim to decrease the computational domain size and thus the simulation time, the symmetric boundary conditions are applied to the horizontal directions to simulate a quarter of a sessile droplet, as shown in Fig. 1(a). The symmetric boundary conditions in this work are adapted from the half-way bounce-back boundary conditions proposed by Lee and Liu [29,56]. Instead of bouncing back at the boundary node $\vec{x}_s$ [Fig. 1(b)], the outgoing particle distribution function f_i reflects back at the symmetric boundary following the rule of specular reflection [Fig. 1(c)]. Thus, we have $f_{\hat{i}}(\vec{x}_s) = f_i(\vec{x}_s)$, where $\hat{i}$ represents the outgoing direction that satisfies $\vec{e}_{\hat{i}} = \vec{e}_i - 2(\vec{e}_i \cdot \vec{n})\vec{n}$ for $\vec{e}_i \cdot \vec{n} \neq 0$, where $\vec{n}$ is the inward normal direction of the boundary. The collision process occurs on the boundary nodes, and their macroscopic properties are updated. The same rule applies for the distribution function g_i. In order to prevent unphysical influences of the boundary nodes during evaporation, the normal derivatives of macroscopic properties are set to zero at the symmetric boundaries.

Due to the presence of off-lattice particles in the system, we introduce ghost particles outside the simulation domain as the mirror images of the real particles with respect to the symmetric boundary, which is similar to the implementation in molecular dynamics simulations with periodic boundary conditions. The mutual forces $\vec{F}^{\mathrm{pp}}$ between the real and ghost particles are taken into account to capture correct particle dynamics in the vicinity of the symmetric boundaries. In addition, the specular reflection is applied to the particles that move across the symmetric boundaries.

The wetting properties of the solid substrate are controlled by the surface energy formulation [27]. The method prescribes the normal derivative of the order parameter at the solid substrate as $(\partial\phi/\partial n)_s = -h/\kappa$, where

$$h = 2(\phi^*)^2\sqrt{2\kappa A}\,\mathrm{sgn}\left(\frac{\pi}{2} - \theta_{\mathrm{eq}}\right)\sqrt{\cos\left(\frac{\alpha}{3}\right)\left[1 - \cos\left(\frac{\alpha}{3}\right)\right]} \tag{9}$$

and $\alpha = \arccos(\sin^2\theta_{\mathrm{eq}})$ for a given equilibrium contact angle θ_{eq}. In multiphase systems without evaporation, the contact line can be readily pinned by replacing θ_{eq} in Eq. (9) with the local apparent contact angle, which is measured at each time step [57]. However, we find that the evaporation model

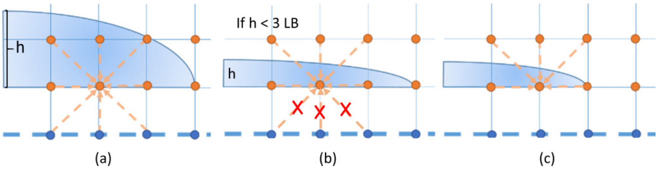

FIG. 2. Schematic diagrams of the pinning and releasing scheme. The orange dots represent the fluid nodes. The blue dots are the solid nodes. The orange arrows indicate the nodes whose macroscopic properties are used when calculating derivatives on the corresponding fluid node. (a) During the pinning stage, the derivatives on the first fluid nodes are calculated from both the inner fluid nodes and the solid nodes. (b) When the droplet height is lower than the critical value, we use only the information on the neighboring fluid nodes but not the solid nodes to calculate the derivatives. (c) After the information from the solid nodes is excluded in the derivative calculation, the contact line starts to recede.

based on the advection-diffusion of the order parameter [46] perturbs the surface free energy and thereby influences the contact angle. As a result, the contact line cannot be pinned steadily through the update of h value according to the instantaneous contact angle.

To overcome this issue, we implemented a new method to pin the contact line under evaporation, which combines the full-way bounce-back scheme on the solid nodes with the isotropic finite difference approximation [32] on the adjacent fluid nodes. In particular, the regular full-way bounce-back boundary condition is applied to the solid nodes. By treating the solid nodes as ghost nodes, the macroscopic properties of the solid nodes are not updated and remain unchanged. As shown in Fig. 2(a), when the contact line needs to be pinned during evaporation, the isotropic finite difference scheme is applied to calculate the derivatives on the fluid nodes immediately adjacent to the solid boundary. Thus, the macroscopic properties of the solid nodes influence the evolution of fluid properties. The constant order parameters on the solid nodes result in contact line pinning. Once the maximum distance between the liquid-vapor interface and the solid substrate reduces to a value comparable to the interfacial thickness (three LB units in this work), the one-sided finite difference method [58] is used instead to exclude the influence of solid nodes [Figs. 2(b) and 2(c)]. Consequently, the pinned contact line is released and thus starts to recede. The motion of the contact line is then governed solely by the surface free energy with the equilibrium contact angle set to be $\theta_{\mathrm{eq}} = 0^\circ$.

D. Simulation parameters

Our computational domain is $40 \times 40 \times 40$ LB units. The two-phase fluid is modeled with dimensionless densities for the liquid phase $\rho_{\mathrm{l}} = 1$ and the vapor phase $\rho_{\mathrm{v}} = 0.1$. The relaxation times are $\tau_f = 0.875$ for the mass-momentum LBE and $\tau_g = 0.7$ for the phase-field LBE. Dynamic viscosity can be calculated from the local density and exhibits a ratio of $10:1$ between the liquid and vapor phases. Other fluid parameters are the mobility parameter $\theta_{\mathrm{M}} = 5$, the interfacial thickness $W = 5$, and surface tension $\sigma = 1 \times 10^{-4}$. The parameters of the particle model are listed as follows: the dimensionless radius $R_{\mathrm{p}} = 0.032$, $\varepsilon_{\mathrm{rep}} = 1.0$, $\varepsilon_{\mathrm{att}} = 1 \times 10^{-7}$, $\lambda = 0.6$, $r_0 = 0.6$, $r_{\mathrm{e}} = 1.2$, $r_{\mathrm{a}} = 0.6$, and $V_0 = 1 \times 10^{-5}$. $k_{\mathrm{B}}T = 1 \times 10^{-7}$ is the default value based on the parametric study, while 1×10^{-6} and 1×10^{-5} are applied to test particle depositions under different Pe numbers. A vertical force with a magnitude of 3.6×10^{-6} is applied to the particles in the vapor phase to mimic particle deposition. The fluid dynamics is solved by the LBM, and the particle dynamics is updated by the BD. One LB fluid time step δt consists of 20 particle time steps. The droplets initially have a radius of $R_{\mathrm{drop}} = 28$ LB units and are centered at the origin. Due to the discrete nature of our particle model, a sufficient total number of particles is vital to obtain statistically and physically meaningful deposition profiles. The total particle number $N_{\mathrm{np}} = 250$ is used in this study, which shows reliable statistics. All droplets require 2×10^5 time steps to reach the equilibrium state before

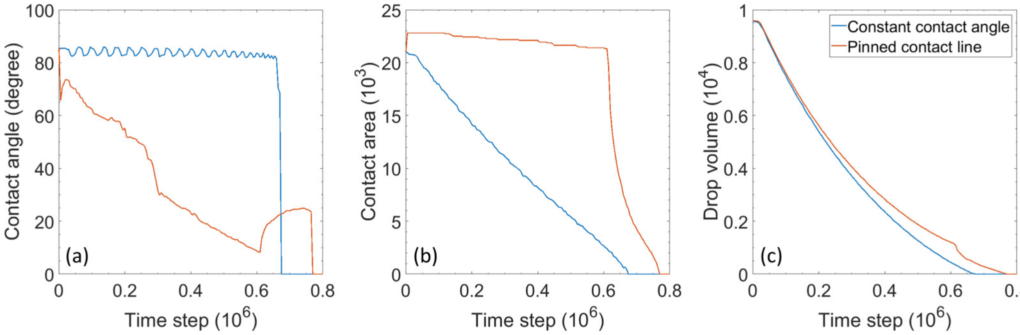

FIG. 3. Time evolutions of the (a) local contact angle, (b) contact area, and (c) droplet volume for the evaporating droplets with a pinned contact line (orange) and a free-slipping contact line (blue) at constant contact angle ($\theta_{\mathrm{eq}} = 90^\circ$).

the introduction of particles and the subsequent evaporation. The evaporation of sessile droplets needs (0.67–0.76) $\times\ 10^6$ time steps to complete dry. All results are generated by an in-house C code.

III. RESULTS AND DISCUSSION

We first examine the effect of the pinning scheme by monitoring the variations of contact angle and contact area as well as the total volume of a sessile droplet during evaporation. The instantaneous local contact angle is calculated using the normal vector of the liquid-vapor interface $\vec{n}_i = \nabla\phi/|\nabla\phi|$ at the contact point [59]. Since the free-energy-based multiphase LBM generates a diffuse interface, we average the values of local contact angles θ_{local} calculated on the points that are both in close proximity to the nominal interface ($\phi = 0$) and located in the first and second layers of fluid nodes adjacent to the solid boundary. The droplet volume is estimated by the total number of lattice nodes in the liquid phase (i.e., $\phi > 0$). The contact area is estimated by the number liquid nodes on the first layer of fluid nodes. Figure 3(a) shows the θ_{local} variation during evaporation for the droplets with a pinned contact line and in the contact angle ($\theta_{\mathrm{eq}} = 90^\circ$) mode. The local contact angle of the droplet with a pinned contact line decreases monotonically to 9° until the release of pinning, while the contact angle of the free-slipping droplet fluctuates near the equilibrium value with small variations. In other words, the pinning scheme allows us to simulate an evaporating droplet with a receding contact angle of 9°. After the release of pinning, the contact line immediately recedes and the contact angle increases. As shown in Fig. 3(b), the contact area of the pinned droplet remains approximately constant, which confirms the pinning of contact line. The contact area of the droplet in the constant contact angle mode exhibits a linear decrease.

The similar droplet volume profiles in Fig. 3(c) suggest that the different dynamics of contact line has no significant influence on the evaporation rate of droplets. However, during the latter stage of evaporation, the droplet with a pinned contact line does evaporate slower than the one with a moving contact line. This behavior is attributed to the increasing influence of the solid nodes when the droplet height reduces. The removal of such influence leads to a sudden change of volume when the contact line is released. These simulation results are consistent with reported experiments [60]. In Fig. 4 we plot the evaporative flux of the two droplets to further the understanding of the evaporation behavior. The evaporative flux in this model is defined based on the Cahn-Hilliard equation as $\vec{j} = -\theta_{\mathrm{M}}\nabla\mu_\phi$ [46]. The droplet with a pinned contact line exhibits differential evaporative flux, which increases from the apex to the contact line along the liquid-vapor interface. In contrast, the free-slipping droplet with $\theta_{\mathrm{eq}} = 90^\circ$ has uniform evaporative flux as shown in Fig. 4(b). Notably, the simulation does not show strong evaporative singularity at the pinned contact line as predicted by the theory [11,21,61,62], which is attributed to the diffuse interface character of the free-energy LBM.

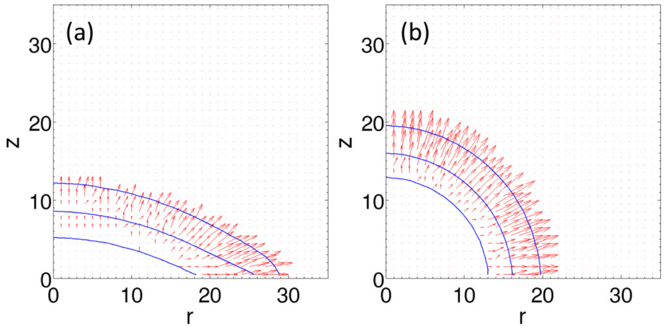

FIG. 4. Instantaneous evaporative flux in the x-o-z plane when $t^* = 0.61$, for the evaporating droplets with (a) a pinned contact line and (b) a free-slipping contact line at constant contact angle ($\theta_{\text{eq}} = 90^\circ$). The blue lines represent the inner boundary, central position, and outer boundary of the interfacial region. The red arrows represent the local evaporative fluxes.

For modeling particle-laden droplets, interface-bound and bulk-dispersed particles are distributed homogeneously in the corresponding regions before evaporation starts, as shown in Figs. 5(a) and 5(b). Due to the prescribed fluid-particle interaction, the interface-bound particles are confined within the liquid-vapor interface, while the bulk-dispersed particles stay in the bulk liquid phase. During evaporation, particle dynamics is dictated by the interplay of advective flow, Brownian motion, fluid-particle interaction, and particle-particle interaction. Both particle trajectories and particle density

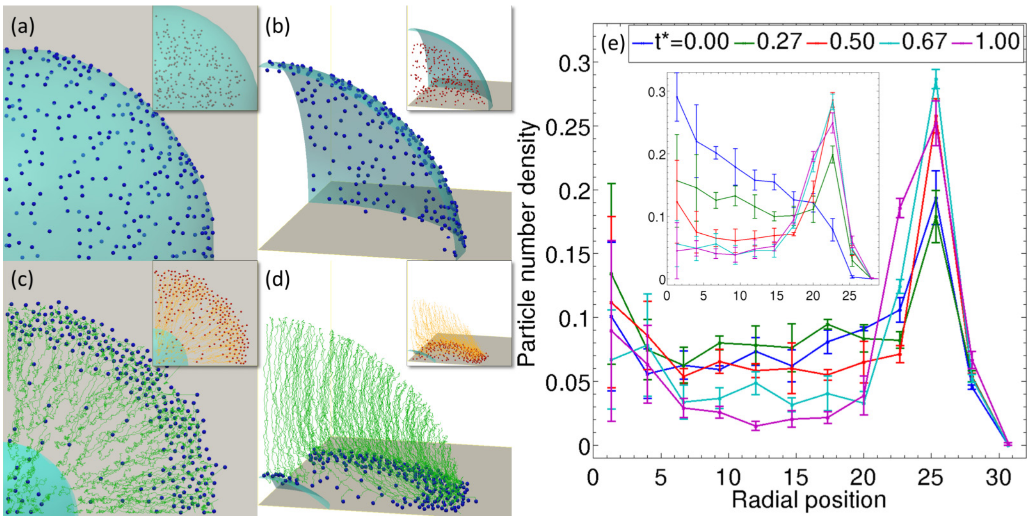

FIG. 5. (a) Top views and (b) side views of a quarter droplet with the interface-bound particles at the beginning of evaporation. (c) Top views and (d) side views of the final deposit after the solvent completely dries. The blue dots represent the particle positions. The green line shows the trajectories of particles during evaporation. (e) Time evolutions of the interface-bound particle number projected per unit area along the radial direction. t^* is the normalized evaporation time with respect to the total time for complete evaporation of the solvent. Error bars denote the standard deviations calculated from four simulations with different random seeds. Notably, the variations of initial particle density along the radial direction in (e) are attributed to the projection of homogeneous particle distribution in the 3D space onto the 2D x-o-y plane. The insets in panels (a) through (e) display the results for the droplet with the bulk-dispersed particles, whose positions are marked by the red dots. The corresponding views of the droplets during evaporation are shown in Movies S1 and S2 [63].

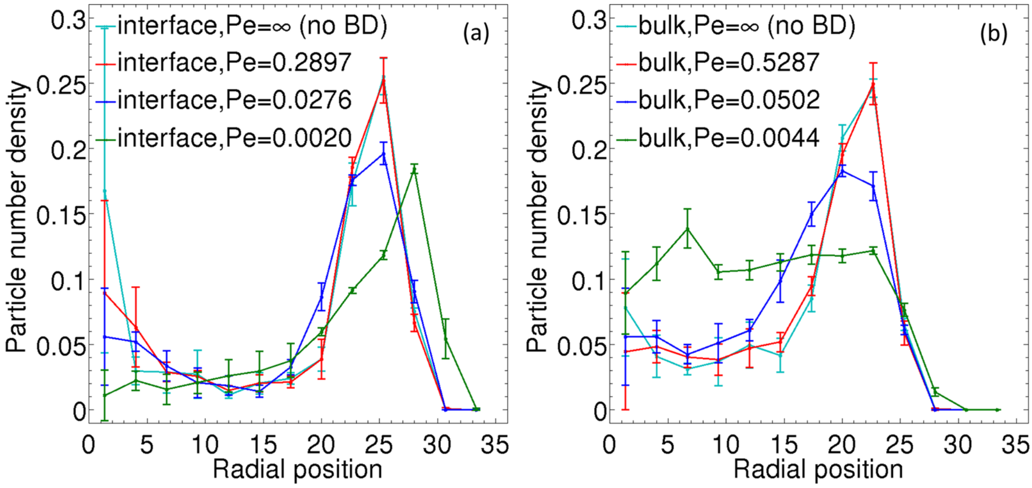

FIG. 6. Density profiles of the final deposits with different Pe numbers for the (a) interface-bound particles and (b) bulk-dispersed particles. Error bars represent the standard deviations calculated from four simulations with different random seeds. D_p in the interfacial region decreases linearly from the bulk value to 0, depending on the particle position. In contrast, it keeps a constant in the liquid phase. This variation leads to different Pe numbers for the bulk-dispersed particles and the interface-bound particles with the same diffusion coefficient defined in the bulk.

profiles show that the particles adsorbed at the interface exhibit different dynamics compared to the particles in the bulk. Surprisingly, Figs. 5(c) and 5(d) reveal that most particles move slowly toward the apex of droplet between $t^* = 0$ and $t^* = 0.27$, except the ones originally near the apex, which do not show noticeable net motion (see Movie S1 [63]). t^* is the normalized evaporation time with respect to the total time for complete evaporation of the solvent. The inward movement slightly increases particle density in the region of $5 < r < 15$ and reduces the peak height around $r = 25$ in Fig. 5(e). As the contact angle decreases, the particles initially migrating to the apex reverse their directions and thus aggregate and deposit near the contact line, which is evident from the density variation. Notably, the particles near the apex still remain stationary, corresponding to the high local density that is invariant during evaporation. The final profile exhibits a significant peak at the contact line representing the coffee ring pattern with a small but unexpected densification at the center as a result of the bidirectional particle transport on the interface. Moreover, a depletion zone located in the region of $10 < r < 15$ can be observed.

In contrast to the interface-bound particles, the radial density of bulk-dispersed particles away from the contact line decreases monotonically throughout the entire evaporation, while the edge density drastically increases. This density evolution indicates that the bulk-dispersed particles consistently migrate toward the contact line, which is confirmed by Movie S2 [63]. Eventually, the final deposition of the bulk-dispersed particles reproduces the classical coffee ring with no center deposit. The trajectories of bulk-dispersed particles closely follow the streamlines predicted by the theoretical solutions [21,62] for evaporating sessile droplets with a pinned contact line.

The Pe number, defined as $\mathrm{Pe} = U R_\mathrm{p}/D_\mathrm{p}$, characterizes the relative magnitude of advective transport and Brownian diffusion of particles, where U is the average particle velocity, R_p is the particle radius, and D_p is the average particle diffusion coefficient. We explore the influence of Pe number on the final particle deposit by tuning the particle diffusion coefficient. Figure 6 shows similar depositions from particles having the reference value of diffusion coefficient [$\mathrm{Pe} = 0.2897$ in (a) and $\mathrm{Pe} = 0.5287$ in (b)] and those with $D_\mathrm{p} = 0$ ($\mathrm{Pe} = \infty$). Thus, weak Brownian motion does not alter the deposition pattern. In typical experiments, the Pe number of the particles dispersed in the bulk during droplet evaporation varies from ∼1 to ∼200 [64,65], which depends on the size and

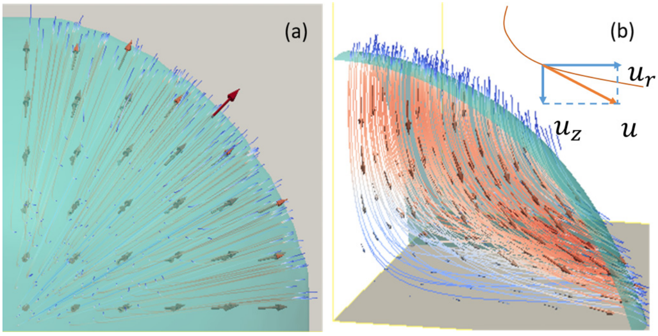

FIG. 7. (a) Top view and (b) side view of the flow vectors and streamlines in a particle-free 3D droplet.

material properties of both droplets and particles. More vigorous Brownian motion with larger D_p reduces radial inhomogeneity. When $\mathrm{Pe} = 0.002$, the density peak of interface-bound particles near the contact line significantly decreases and widens. The peak even shifts outward, which is attributed to weakened interfacial confinement under strong Brownian diffusion. Notably, our model considers no fluid-particle interaction force $\vec{F}^\mathrm{f}$ in the vapor phase. The interface-bound particles can enter the vapor region easily with strong Brownian motion and thus widen their distribution across the interface. For the bulk-dispersed particles, the density peak also becomes lower and broader as the Pe number decreases, as shown in Fig. 6(b).

To understand the intriguing dynamics of interface-bound particles, we present the flow field analysis based on an evaporating particle-free droplet with a pinned contact line. Due to the diffuse interface produced by the free-energy LBM, there are multiple interfacial velocity points for each radial position. Figure 7 shows that fluid velocity vectors point downward and outward (i.e., from the droplet apex toward the contact line) with magnitudes increasing from the center to the contact line. Figures 8 and 9 plot the two-dimensional flow field extracted from the *x*-*o*-*z* plane of 3D simulation results. We also plot the analytical solution for the Stokes flow inside an evaporating droplet given by Masoud and Felske [62,66] for comparison. At the early stage of evaporation (i.e., at a large contact angle), the simulation velocities in the bulk are highly consistent with the theoretical prediction, regarding both direction and magnitude, as shown in Figs. 8 and 10(a). As the contact angle reduces upon evaporation, the magnitude of simulation velocities deviates progressively from the theory (see

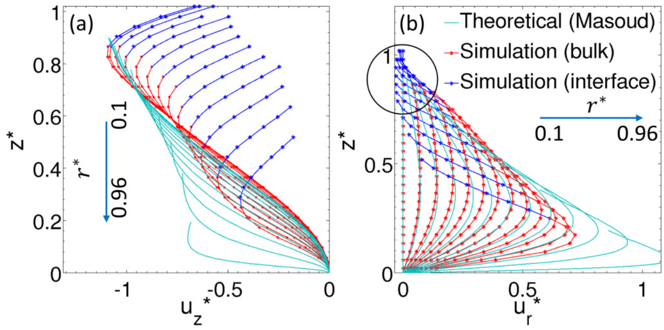

FIG. 8. Profiles of the (a) vertical velocity components u_z^* and (b) radial velocity components u_r^* at different radial position when the local contact angle is $\theta_\mathrm{local} = 84^\circ$. The interfacial flow (blue dots) from the simulation results is connected with the bulk flow (red dots) at the same radial position. The analytical flow field (cyan solid lines) within the liquid phase is plotted at the same time step for the same contact angle. The black circle in (d) highlights the negative radial velocities. The numerical velocity profiles start from $z = 1$, because the macroscopic velocity is not calculated at $z = 0$.

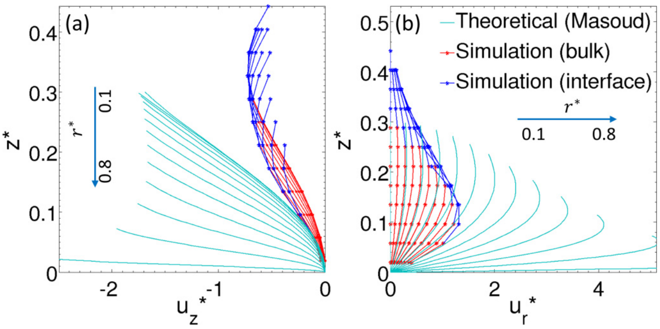

FIG. 9. Profiles of the (a) vertical velocity components u_z^* and (b) radial velocity components u_r^* at different radial position when the local contact angle is $\theta_{\text{local}} = 33^\circ$. Other details are the same as Fig. 8.

Fig. 9), despite the well-aligned directions shown in Fig. 10(b). The large discrepancy between the analytical solution and simulation results at a low contact angle could be induced by two reasons. First, the theoretical solution [21] is derived for the Stokes flow with an approximate evaporative flux, while the LBM method fully recovers the continuity and Navier-Stokes equations. Second, although our model captures the differential evaporation along the surface of pinned droplet as shown in Fig. 4(a), the evaporative flux near the contact line does not show strong singular behavior when the contact angle is small due to the diffuse-interface model, in contrast to the theory [11,21,61,62]. We speculate that the absence of an evaporative singularity in the simulation yields weaker bulk advection in the droplet.

At a certain radial position, the interfacial flow is weaker than the bulk flow close to the interface when the contact angle is large, as shown in Fig. 8. The simulation results reveal small but indiscernible radial velocities pointing to the droplet apex. The negative velocity occurs near the outer boundary of the interfacial region at small r, which is relevant only to particles near the apex. This negative velocity contributes to the inward particle migration at the early stage of evaporation. As the droplet contact angle decreases, the maximum velocity shifts into the interfacial region and the negative radial velocities in the interfacial region vanish. This flow variation explains why the "rush hour" effect [67] also appears for the interface-bound particles at the end of drying. Figure 11 shows the variation of particle distribution modeled as a one-dimensional advection process in toroidal coordinates [66], which confirms the influence of interfacial flow on the interface-bound particles.

However, the inward radial flow carries only particles already near the apex to the center, while other particles should be advected to the contact angle by the outward flow. We further probe additional effects that yield the inward movement of particles away from the droplet apex. We speculate that the downward displacement of evaporating droplet surface also plays an important

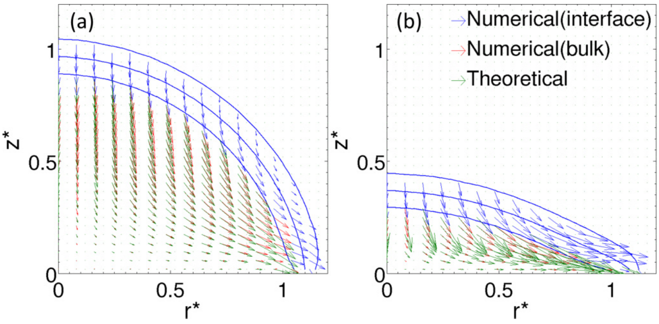

FIG. 10. Flow fields in the x-o-z plane when local contact angles are (a) $\theta_{\text{local}} = 84^\circ$ and (b) $\theta_{\text{local}} = 33^\circ$.

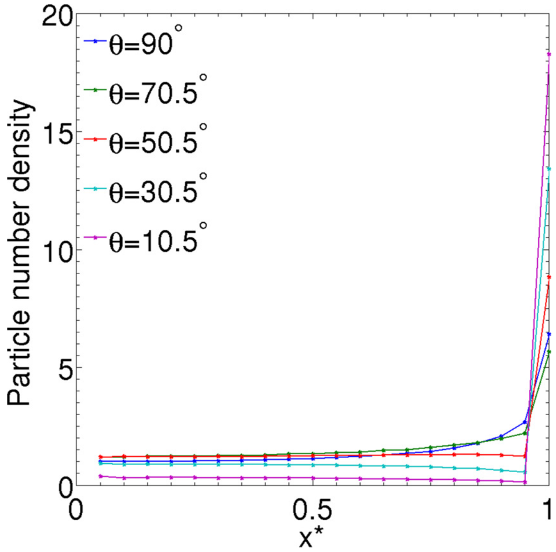

FIG. 11. Time evolution of the 1D theoretical particle density profile obtained by the theoretical solution in Ref. [66].

role in the dynamics of particles confined at the interface. As shown in the inset of Fig. 12, with only fluid-particle interaction force $\vec{F}^{\mathrm{p}}$, particle trajectories closely follow the θ axis [62] of a toroidal coordinate system with the origin at the contact line. In other words, the moving interface effectively maps particles to the substrate. Time evolution of particle density profiles confirms that the interface-bound particles migrate toward the apex under the mapping of the drying surface. When the interfacial flow is weak at the startup of evaporation, the inward particle motion is mainly induced

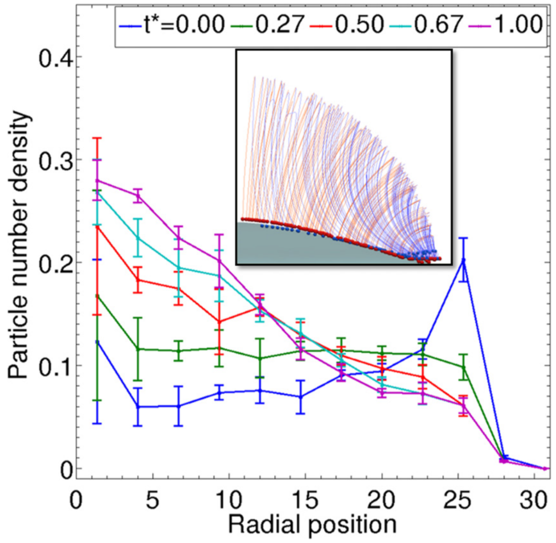

FIG. 12. Time evolutions of the projected density of the interface-bound particles along the radial direction without advection along the droplet surface. The inset shows a comparison of the projected particle trajectories in the r-o-z plane for non-Brownian simulations of the interface-bound particles with (blue) and without (red) advection.

by the physical constraint of droplet surface. However, this backward motion is present only for a short period. As evaporation continues, the interfacial advection quickly enhances and overpowers the surface-induced displacement, therefore reversing the direction of particle motion.

IV. CONCLUSIONS

In this paper, we apply a 3D LB-BD model to simulate particle self-assembly and deposition in drying droplets. We find that the particle dynamics at the liquid-vapor interface are different from that in the liquid phase. The deposit of the interface-bound particles exhibits a small density enhancement at the center of the droplet footprint after drying, in addition to the pronounced coffee ring pattern. In order to explore the formation mechanism for this center deposit, we interrogate the flow field induced by evaporation, especially the interfacial flow on the droplet surface. The interfacial flow is weaker than the bulk flow at the early stage of evaporation, however, directing to the droplet center in the region near the apex. Furthermore, the constraint of the evaporating liquid-vapor interface generates inward displacement for all interface-bound particles. Together, the advective flow along the droplet surface and the downward motion of the surface itself yield the enhanced density at the center.

This work provides important hydrodynamic insight into particle assembly at the liquid-vapor interface induced by isothermal and quasisteady droplet evaporation. The present model does not capture the thermal and surfactant Marangoni effects from the evaporative cooling, substrate heating, and surfactant contamination. The particle dynamics at the liquid-vapor interface could be even more complicated with those effects considered. For example, the presence of the Marangoni convection can significantly disturb the surface flow or even reverse it. Due to the interfacial confinement, the surface-adsorbed particles can experience more pronounced influences from the surface advection than the particles in the bulk, where the advection toward the contact line will eventually prevail. We envision that harnessing the interfacial flow and surface confinement for the surface-active particles can provide a new avenue for controlling deposition pattern from drying droplets for various applications.

ACKNOWLEDGMENTS

The authors would like to acknowledge financial support from the U.S. National Science Foundation under Grant No. CMMI-1538090. Generous allocations of computing time were provided by the Watson Data Center at Binghamton University. We thank Saeed Jafari Kang and Prof. Hassan Masoud for providing the analytical solution of Stokes flow and a 1D solution of particle distribution at the interface. We also thank Profs. Paul R. Chiarot and Timothy J. Singler for helpful conversations.

---

[1] B. A. Parviz, D. Ryan, and G. M. Whitesides, Using self-assembly for the fabrication of nano-scale electronic and photonic devices, IEEE Trans. Adv. Packag. **26**, 233 (2003).
[2] B. Dan, T. B. Wingfield, J. S. Evans, F. Mirri, C. L. Pint, M. Pasquali, and I. I. Smalyukh, Templating of self-alignment patterns of anisotropic gold nanoparticles on ordered SWNT macrostructures, ACS Appl. Mater. Interfaces **3**, 3718 (2011).
[3] Y. Cai and B. M. Z. Newby, Marangoni flow-induced self-assembly of hexagonal and stripelike nanoparticle patterns, J. Am. Chem. Soc. **130**, 6076 (2008).
[4] K. Sefiane, Patterns from drying drops, Adv. Colloid Interface Sci. **206**, 372 (2014).
[5] M. Kuang, L. Wang, and Y. Song, Controllable printing droplets for high-resolution patterns, Adv. Mater. **26**, 6950 (2014).
[6] G. Shambat, S. Rajasekhar Kothapalli, A. Khurana, J. Provine, T. Sarmiento, K. Cheng, Z. Cheng, J. Harris, H. Daldrup-Link, S. Sam Gambhir, and J. Vučković, A photonic crystal cavity-optical fiber tip nanoparticle sensor for biomedical applications, Appl. Phys. Lett. **100**, 213702 (2012).

[7] T. Kajiya, D. Kaneko, and M. Doi, Dynamical visualization of “coffee stain phenomenon” in droplets of polymer solution via fluorescent microscopy, Langmuir **24**, 12369 (2008).

[8] S. Mishra, K. L. Barton, A. G. Alleyne, P. M. Ferreira, and J. A. Rogers, High-speed and drop-on-demand printing with a pulsed electrohydrodynamic jet, J. Micromech. Microeng. **20**, 95026 (2010).

[9] Y. L. Kong, I. A. Tamargo, H. Kim, B. N. Johnson, M. K. Gupta, T. W. Koh, H. A. Chin, D. A. Steingart, B. P. Rand, and M. C. McAlpine, 3D printed quantum dot light-emitting diodes, Nano Lett. **14**, 7017 (2014).

[10] E. L. Talbot, H. N. Yow, L. Yang, A. A. Berson, S. R. Biggs, and C. D. Bain, Printing small dots from large drops, ACS Appl. Mater. Interfaces **7**, 3782 (2015).

[11] R. D. Deegan, O. Bakajin, T. F. Dupont, G. Huber, S. R. Nagel, and T. A. Witten, Capillary flow as the cause of ring stains from dried liquid drops, Nature (London) **389**, 827 (1997).

[12] X. Man and M. Doi, Ring to Mountain Transition in Deposition Pattern of Drying Droplets, Phys. Rev. Lett. **116**, 066101 (2016).

[13] P. J. Sáenz, A. W. Wray, Z. Che, O. K. Matar, P. Valluri, J. Kim, and K. Sefiane, Dynamics and universal scaling law in geometrically-controlled sessile drop evaporation, Nat. Commun. **8**, 14783 (2017).

[14] L. Cui, J. Zhang, X. Zhang, Y. Li, Z. Wang, H. Gao, T. Wang, S. Zhu, H. Yu, and B. Yang, Avoiding coffee ring structure based on hydrophobic silicon pillar arrays during single-drop evaporation, Soft Matter **8**, 10448 (2012).

[15] H. Hu and R. G. Larson, Marangoni effect reverses coffee-ring depositions, J. Phys. Chem. B **110**, 7090 (2006).

[16] H. Kim, F. Boulogne, E. Um, I. Jacobi, E. Button, and H. A. Stone, Controlled Uniform Coating from the Interplay of Marangoni Flows and Surface-Adsorbed Macromolecules, Phys. Rev. Lett. **116**, 124501 (2016).

[17] T. Still, P. J. Yunker, and A. G. Yodh, Surfactant-induced Marangoni eddies alter the coffee-rings of evaporating colloidal drops, Langmuir **28**, 4984 (2012).

[18] M. Anyfantakis, Z. Geng, M. Morel, S. Rudiuk, and D. Baigl, Modulation of the coffee-ring effect in particle/surfactant mixtures: The importance of particle–interface interactions, Langmuir **31**, 4113 (2015).

[19] P. J. Yunker, T. Still, M. A. Lohr, and A. G. Yodh, Suppression of the coffee-ring effect by shape-dependent capillary interactions, Nature (London) **476**, 308 (2011).

[20] W. Han and Z. Lin, Learning from “coffee rings”: Ordered structures enabled by controlled evaporative self-assembly, Angew. Chemie Intl. Ed. **51**, 1534 (2012).

[21] H. Hu and R. G. Larson, Analysis of the microfluid flow in an evaporating sessile droplet, Langmuir **21**, 3963 (2005).

[22] W. Chen, J. Koplik, and I. Kretzschmar, Molecular dynamics simulations of the evaporation of particle-laden droplets, Phys. Rev. E **87**, 052404 (2013).

[23] Á. G. Marín, H. Gelderblom, D. Lohse, and J. H. Snoeijer, Order-to-Disorder Transition in Ring-Shaped Colloidal Stains, Phys. Rev. Lett. **107**, 085502 (2011).

[24] N. A. Brown, Y. Zhu, A. Li, M. Zhao, X. Yong, and P. R. Chiarot, Structure of electrospray printed deposits for short spray times, J. Micro Nano-Manufacturing **5**, 40906 (2017).

[25] A. Marin, R. Liepelt, M. Rossi, and C. J. Kähler, Surfactant-driven flow transitions in evaporating droplets, Soft Matter **12**, 1593 (2016).

[26] M. R. Swift, E. Orlandini, W. R. Osborn, and J. M. Yeomans, Lattice Boltzmann simulations of liquid-gas and binary fluid systems, Phys. Rev. E **54**, 5041 (1996).

[27] A. J. Briant, A. J. Wagner, and J. M. Yeomans, Lattice Boltzmann simulations of contact line motion. I. Liquid-gas systems, Phys. Rev. E **69**, 031602 (2004).

[28] H. W. W. Zheng, C. Shu, and Y. T. T. Chew, A lattice Boltzmann model for multiphase flows with large density ratio, J. Comput. Phys. **218**, 353 (2006).

[29] T. Lee and L. Liu, Lattice Boltzmann simulations of micron-scale drop impact on dry surfaces, J. Comput. Phys. **229**, 8045 (2010).

[30] X. He, S. Chen, and R. Zhang, A lattice Boltzmann scheme for incompressible multiphase flow and its application in simulation of Rayleigh–Taylor instability, J. Comput. Phys. **663**, 642 (1999).

[31] T. Inamuro, T. Ogata, S. Tajima, and N. Konishi, A lattice Boltzmann method for incompressible two-phase flows with large density differences, J. Comput. Phys. **198**, 628 (2004).

[32] T. Lee and C.-L. L. Lin, A stable discretization of the lattice Boltzmann equation for simulation of incompressible two-phase flows at high density ratio, J. Comput. Phys. **206**, 16 (2005).

[33] Y. Y. Yan and Y. Q. Zu, A lattice Boltzmann method for incompressible two-phase flows on partial wetting surface with large density ratio, J. Comput. Phys. **227**, 763 (2007).

[34] G. Falcucci, S. Ubertini, and S. Succi, Lattice Boltzmann simulations of phase-separating flows at large density ratios: The case of doubly-attractive pseudo-potentials, Soft Matter **6**, 4357 (2010).

[35] Y. Q. Zu and S. He, Phase-field-based lattice Boltzmann model for incompressible binary fluid systems with density and viscosity contrasts, Phys. Rev. E **87**, 043301 (2013).

[36] J. Y. Shao, C. Shu, H. B. Huang, and Y. T. Chew, Free-energy-based lattice Boltzmann model for the simulation of multiphase flows with density contrast, Phys. Rev. E **89**, 033309 (2014).

[37] Y. Wang, C. Shu, H. B. Huang, and C. J. Teo, Multiphase lattice Boltzmann flux solver for incompressible multiphase flows with large density ratio, J. Comput. Phys. **280**, 404 (2015).

[38] J. Y. Shao and C. Shu, A hybrid phase field multiple relaxation time lattice Boltzmann method for the incompressible multiphase flow with large density contrast, Int. J. Numer. Methods Fluids **77**, 526 (2015).

[39] A. Fakhari, M. Geier, and T. Lee, A mass-conserving lattice Boltzmann method with dynamic grid refinement for immiscible two-phase flows, J. Comput. Phys. **315**, 434 (2016).

[40] T. Inamuro, T. Yokoyama, K. Tanaka, and M. Taniguchi, An improved lattice Boltzmann method for incompressible two-phase flows with large density differences, Comput. Fluids **137**, 55 (2016).

[41] M. Zhao and X. Yong, Modeling evaporation and particle assembly in colloidal droplets, Langmuir **33**, 5734 (2017).

[42] R. Verberg, J. M. Yeomans, and A. C. Balazs, Modeling the flow of fluid/particle mixtures in microchannels: Encapsulating nanoparticles within monodisperse droplets, J. Chem. Phys. **123**, 224706 (2005).

[43] Y. Ma, A. Bhattacharya, O. Kuksenok, D. Perchak, and A. C. Balazs, Modeling the transport of nanoparticle-filled binary fluids through micropores, Langmuir **28**, 11410 (2012).

[44] C. Xie, J. Zhang, V. Bertola, and M. Wang, Lattice Boltzmann modeling for multiphase viscoplastic fluid flow, J. Non-Newton. Fluid Mech. **234**, 118 (2016).

[45] Y. Liu, A. Bhattacharya, O. Kuksenok, X. He, M. Aizenberg, J. Aizenberg, and A. C. Balazs, Computational modeling of oscillating fins that "catch and release" targeted nanoparticles in bilayer flows, Soft Matter **12**, 1374 (2016).

[46] R. Ledesma-Aguilar, D. Vella, and J. M. Yeomans, Lattice-Boltzmann simulations of droplet evaporation, Soft Matter **10**, 8267 (2014).

[47] H. Safari, M. H. Rahimian, and M. Krafczyk, Extended lattice Boltzmann method for numerical simulation of thermal phase change in two-phase fluid flow, Phys. Rev. E **88**, 013304 (2013).

[48] H. Safari, M. H. Rahimian, and M. Krafczyk, Consistent simulation of droplet evaporation based on the phase-field multiphase lattice Boltzmann method, Phys. Rev. E **90**, 033305 (2014).

[49] M. Mohammadi-Shad and T. Lee, Phase-field lattice Boltzmann modeling of boiling using a sharp-interface energy solver, Phys. Rev. E **96**, 013306 (2017).

[50] D. Hessling, Q. Xie, and J. Harting, Diffusion dominated evaporation in multicomponent lattice Boltzmann simulations, J. Chem. Phys. **146**, 1 (2017).

[51] R. Ledesma-Aguilar, G. Laghezza, J. M. Yeomans, and D. Vella, Using evaporation to control capillary instabilities in micro-systems, Soft Matter **13**, 8947 (2017).

[52] K. M. Schweigler, M. Ben Said, S. Seifritz, M. Selzer, and B. Nestler, Experimental and numerical investigation of drop evaporation depending on the shape of the liquid/gas interface, Int. J. Heat Mass Transf. **105**, 655 (2017).

[53] H. Hu and R. G. Larson, Analysis of the effects of marangoni stresses on the microflow in an evaporating sessile droplet, Langmuir **21**, 3972 (2005).

[54] M. Majumder, C. S. Rendall, J. A. Eukel, J. Y. L. Wang, N. Behabtu, C. L. Pint, T. Y. Liu, A. W. Orbaek, F. Mirri, J. Nam, A. R. Barron, R. H. Hauge, H. K. Schmidt, and M. Pasquali, Overcoming the "coffee-stain" effect by compositional marangoni-flow-assisted drop-drying, J. Phys. Chem. B **116**, 6536 (2012).

[55] X. Xu and J. Luo, Marangoni flow in an evaporating water droplet, Appl. Phys. Lett. **91**, 124102 (2007).

[56] T. Lee and L. Liu, Wall boundary conditions in the lattice Boltzmann equation method for nonideal gases, Phys. Rev. E **78**, 017702 (2008).

[57] L. Wang, H. Huang, and X.-Y. Lu, Scheme for contact angle and its hysteresis in a multiphase lattice Boltzmann method, Phys. Rev. E **87**, 013301 (2013).

[58] J. C. Strikwerda, *Finite Difference Schemes and Partial Differential Equations*, 2nd ed. (Society for Industrial and Applied Mathematics, Philadelphia, PA, 2004).

[59] H. Ding and P. D. M. Spelt, Wetting condition in diffuse interface simulations of contact line motion, Phys. Rev. E **75**, 046708 (2007).

[60] C. T. Burkhart, K. L. Maki, and M. J. Schertzer, Effects of interface velocity, diffusion rate, and radial velocity on colloidal deposition patterns left by evaporating droplets, J. Heat Transfer **139**, 111505 (2017).

[61] B. J. Fischer, Particle convection in an evaporating colloidal droplet, Langmuir **18**, 60 (2002).

[62] H. Masoud and J. D. Felske, Analytical solution for Stokes flow inside an evaporating sessile drop: Spherical and cylindrical cap shapes, Phys. Fluids **21**, 42102 (2009).

[63] See Supplemental Material at http://link.aps.org/supplemental/10.1103/PhysRevFluids.3.034201 for top and side views of particle motion at the liquid-vapor interface of the drying droplet with particle trajectories (Movie S1) and for top and side views of particle motion in the bulk of the drying droplet with particle trajectories (Movie S2).

[64] Y. Wei, Effect of particles on evaporation of droplet containing particles, Ph.D. thesis, University of Central Florida, 2015.

[65] G. Derkachov, K. Kolwas, D. Jakubczyk, M. Zientara, and M. Kolwas, Drying of a microdroplet of water suspension of nanoparticles: From surface aggregates to microcrystal, J. Phys. Chem. C **112**, 16919 (2008).

[66] S. Jafari Kang, V. Vandadi, J. D. Felske, and H. Masoud, Alternative mechanism for coffee-ring deposition based on active role of free surface, Phys. Rev. E **94**, 063104 (2016).

[67] Á. G. Marín, H. Gelderblom, D. Lohse, and J. H. Snoeijer, Rush-hour in evaporating coffee drops, Phys. Fluids **23**, 9 (2011).